ORIGINAL PAPER

Compressibility of nanocrystalline forsterite

Hélène Couvy · Jiuhua Chen · Vadym Drozd

Abstract We established an equation of state for nanocrystalline forsterite using multi-anvil press and diamond anvil cell. Comparative high-pressure and high-temperature experiments have been performed up to 9.6 GPa and 1,300°C. We found that nanocrystalline forsterite is more compressible than macro-powder forsterite. The bulk modulus of nanocrystalline forsterite is equal to 123.3 ($\pm$3.4) GPa whereas the bulk modulus of macro-powder forsterite is equal to 129.6 ($\pm$3.2) GPa. This difference is attributed to a weakening of the elastic properties of grain boundary and triple junction and their significant contribution in nanocrystalline sample compare to the bulk counterpart. The bulk modulus at zero pressure of forsterite grain boundary was determined to be 83.5 GPa.

Keywords Equation of state · Nanocrystalline mineral · High-pressure high-temperature experiments · Subducting slab

Introduction

Grain size and grain shape parameters have a great influence on the physical properties of minerals as well as on geophysical processes. Rheological properties of minerals are strongly dependent on grain size (Frost and Ashby 1982). With the decrease of grain size the deformation mechanism passes from dislocation-controlled creep to diffusion-controlled creep. Physical properties of earth's minerals are usually studied at micro- or millimetric scales but not at nanometric scale. Even though nanocrystalline minerals might have an important influence on geological processes (Hochella et al. 2008 for review), they are very poorly studied. Despite their limited occurrences in the crust and the mantle, studies show their importance in geophysics. For instance, mechanical grinding of rocks associated with earthquakes can generate gouge of nanoparticles, which are themselves likely to be important in fault mechanics (Wilson et al. 2005). In the context of subducting slab, experiments show presence of nanoparticles of ringwoodite, which is assumed to play an important role in deep-focus earthquakes (Burnley et al. 1991; Green and Burnley 1989).

This work presents results on compressibility of nanocrystalline forsterite (Mg_2SiO_4). An equation of state of nanocrystalline forsterite has been established and the difference of compressibility with macro-powder sample has been discussed. This is, to our knowledge, the first study on equation of state of nanocrystalline silicate.

Experimental procedure

Nanocrystalline forsterite (nc-Fo) was synthesized following the sol–gel process described by Saberi et al. (2007). The final calcination was performed at 1,073 K for 6 h under a flow oxygen in order to remove the residual carbon. Macro-powder forsterite (m-Fo) was synthesized from a stoichiometric mixture of SiO_2 and MgO, finely grinded and fired at 1,000°C for several hours. Compression data of both nc-Fo and m-Fo were collected using two different experimental set-ups, diamond anvil cell (DAC) and multi-anvil press (MAP), for a good range of pressures and temperatures.

H. Couvy (✉) · J. Chen · V. Drozd
Department of Mechanical and Materials Engineering,
The Center for the Study of Matter at Extreme Conditions,
Florida International University, Miami, FL 33199, USA
e-mail: helene.couvy@gmail.com

DAC experiments

A Mao-Bell cell with 400 μm anvil culet and 270 μm thick stainless steel gasket pre-indented to 50 μm thickness was used (Mao et al. 1979). The sample (nc-Fo or m-Fo) was loaded in a sample chamber of about 180 μm in diameter. Silicone oil (Aldrich, 5 cSt viscosity) was used as pressure-transmitting medium. Shen et al. (2004) showed that silicone oil with a viscosity of 1 cSt provides a quasi-hydrostatic medium as good as 4:1 alcohol mixture up to 20 GPa. In a more recent study, Klotz et al. (2009) has identified a typical gradient of 0.4 GPa below 12 GPa at ambient temperature. In situ X-ray diffraction experiments were conducted at the X17B3 beamline of the National Synchrotron Light Source (NSLS), Brookhaven National Light Source. In each experiment, one 1 μm chip of ruby was loaded into DAC for pressure measurement using a ruby R1 line fluorescence method (Mao et al. 1986). After collecting a diffraction spectrum at ambient conditions, the pressure was increased stepwise and X-ray diffraction patterns were collected at each step for 30 min. Sample pressure was measured before and after the sample diffraction pattern, and an average of the measured pressures is used in data processing (Table 1). Good quality diffraction data were collected up to a maximum pressure of 7.6 GPa. Above this pressure, diffraction signal from nc-Fo sample became much weaker, and even one-hour exposure time still produced a too low signal-to-background ratio for reasonable cell parameter refinements. The diffraction data were analyzed using Fit2D combined with MAUD for cell refinement (Lutterotti et al. 1999).

MAP experiments

The cubic-anvil MAP SAM85 at X17B2 beam line of NSLS was used for in situ high pressure and temperature X-ray diffraction. Amorphous boron mixed with epoxy resin (4:1) was used as pressure medium (Fig. 1). The cell assembly was made of relatively soft materials in order to limit non-hydrostatic stress during the experiment. For direct comparison under the same experimental conditions, a layer of m-Fo and a layer of nc-Fo (mixed with boron nitride powder to avoid grain growth) separated by a layer of NaCl + BN mixture were loaded in a BN sample capsule of 1 mm in diameter and 2 mm in length. The cell pressure was derived from the measured volume of NaCl using X-ray diffraction and Decker scale (Decker 1971), which has an accuracy better than 2% for our experimental P-T ranges (Decker 1965, 1971; Mueller et al. 2003). Temperature was directly measured using a W3%Re–W25%Re thermocouple. The experimental procedure was the following: the press load was increased to 60 ton and the temperature was raised to 1,573 K to

anneal the sample stress developed during compression. According to Weidner et al. (1992, 1994) and Wang et al. (1998) the deviatoric stress level becomes undetectable for temperature as low as 723 K. The annealing temperature was maintained for just few minutes to avoid grain growth. After annealing, the temperature was decreased to 1,273 K, and then to ambient temperature by 200 K step. The heating/cooling cycle was repeated at 10-ton load interval from 60 to 0 ton during decompression. Energy dispersive X-ray diffraction spectra of nc-Fo, m-Fo and NaCl were collected at each step of cooling and decompression. The cell parameters of nc-Fo, m-Fo and NaCl were extracted from the diffraction spectra using the software Plot85 (Baldwin 1990).

Results and discussion

X-ray diffraction patterns of m-Fo and nc-Fo before experiments (Fig. 2) were collected from 15° to 60° (2θ) using Siemens D5000 diffractometer (Cu Kα radiation). nc-Fo appears to be well crystallized and exhibits peaks broadening resulting from the nanoparticle size of the sample (see subview of Fig. 2 for a typical peak broadening of nc-Fo compare to m-Fo).

The grain size of m-Fo was measured to 5 μm from previous experiments in similar conditions using scanning electron microscopy. Using the energy dispersive spectra collected at X17B2 and the Scherrer equation (Gerward et al. 1976), the crystallite size of nc-Fo was determined based on the variation of peak width of (021), (002) (130) (131) and (112) as a function of photon energy. Gerward et al. (1976) show that the crystallite size determined using Scherrer equation is in very good agreement with the size obtained using electron microscope. The technique has been applied for grain size determination for nanocrystalline MgO sample at high pressure using the following scheme (Chen et al. 2005). Line broadening at half the maximum intensity of a Gaussian profile (β) can be caused by elastic strain (β_D) or small grain size (β_S) (Willets 1965):

$$\beta^2 = \beta_D^2 + \beta_S^2 \tag{1}$$

In case of energy dispersive diffraction, β_D and β_S can be expressed as:

$$\beta_D = 2eE \tag{2a}$$

$$\beta_S = \frac{K(^1\!/_2 hc)}{L \sin \theta_0} \tag{2b}$$

where e is the approximate upper limit of strain, E is the X-ray photon energy, K is a Scherrer constant that we set at 0.9, h is the Plank's constant, c is the velocity of light, L is the average crystallite size, $2\theta_0$ is the fixed scattering angle.

Table 1 Experimental conditions and results (see text for uncertainties)

T (K)	P (GPa)	m-Fo (DAC)				nc-Fo (DAC)			
		a (Å)	b (Å)	c (Å)	V (Å³)	a (Å)	b (Å)	c (Å)	V (Å³)
RT	0.3	4.760	10.195	5.985	290.4	–	–	–	–
	0.8	–	–	–	–	4.749	10.198	5.981	289.7
	2.5	4.733	10.127	5.949	285.1	–	–	–	–
	4.5	4.719	10.070	5.922	281.4	–	–	–	–
	7.6	–	–	–	–	4.680	9.973	5.892	275.0
	8.1	4.717	9.942	5.868	275.165	–	–	–	–

T (K)	P (GPa)	m-Fo (MAP)				nc-Fo (MAP)			
		a (Å)	b (Å)	c (Å)	V (Å³)	a (Å)	b (Å)	c (Å)	V (Å³)
RT	0.0	4.743	10.204	5.997	290.2	4.747	10.199	5.993	290.2
	2.3	4.737	10.119	5.957	285.5	4.735	10.137	5.939	285.1
	3.7	4.723	10.079	5.936	282.6	4.729	10.098	5.906	282.0
	5.1	4.717	10.043	5.914	280.2	4.713	10.067	5.886	279.3
	5.8	4.707	10.014	5.904	278.3	–	–	–	–
	6.5	4.706	10.003	5.901	277.8	4.714	10.024	5.873	277.5
	7.8	4.712	9.980	5.869	276.0	–	–	–	–
473	2.8	4.736	10.124	5.957	285.6	4.738	10.140	5.935	285.1
	4.2	4.724	10.074	5.940	282.7	4.731	10.098	5.907	282.2
	5.5	4.716	10.050	5.913	280.3	4.723	10.053	5.898	280.1
	6.2	4.708	10.020	5.906	278.6	4.716	10.029	5.878	278.0
	6.9	4.701	9.999	5.891	276.9	4.708	10.015	5.868	276.7
	7.4	–	–	–	–	4.711	10.006	5.865	276.5
673	3.3	4.737	10.127	5.958	285.8	4.739	10.147	5.933	285.3
	4.8	4.723	10.079	5.938	282.7	4.735	10.095	5.912	282.6
	6.1	4.715	10.044	5.919	280.3	4.725	10.061	5.898	280.4
	6.9	4.711	10.021	5.904	278.7	4.721	10.019	5.898	279.0
	7.6	4.701	9.998	5.892	276.9	4.709	10.018	5.863	276.6
	8.0	4.712	9.994	5.889	277.3	4.712	10.010	5.871	276.9
873	3.7	4.739	10.134	5.961	286.3	4.747	10.153	5.933	286.0
	5.3	4.727	10.083	5.938	283.0	4.740	10.104	5.906	282.8
	6.6	4.720	10.047	5.920	280.7	4.729	10.064	5.899	280.7
	7.4	4.713	10.024	5.906	279.0	4.716	10.039	5.883	278.5
	8.1	4.705	10.002	5.894	277.4	4.714	10.018	5.869	277.1
	8.6	4.713	9.997	5.892	277.6	4.713	10.015	5.870	277.0
1,073	5.6	4.722	10.062	5.921	281.3	4.738	10.116	5.905	283.1
	6.8	4.737	10.137	5.967	286.5	4.728	10.073	5.897	280.8
	7.8	4.728	10.089	5.946	283.6	4.720	10.043	5.883	278.9
	8.5	4.718	10.029	5.907	279.5	4.715	10.023	5.867	277.2
	9.0	4.714	10.001	5.896	278.0	4.714	10.021	5.873	277.4
1,273	4.0	4.745	10.167	5.974	288.2	4.761	10.194	5.931	287.8
	5.8	4.732	10.099	5.949	284.3	4.741	10.123	5.909	283.6
	7.1	4.724	10.071	5.925	281.9	4.729	10.079	5.902	281.3
	8.0	4.720	10.033	5.912	279.9	4.724	10.051	5.883	279.3
	8.8	4.708	10.014	5.900	278.1	4.718	10.024	5.876	277.9
	9.5	–	–	–	–	4.717	10.016	5.872	277.5
1,573	5.9	4.739	10.129	5.960	286.1	4.736	10.125	5.956	285.6
	7.4	4.728	10.083	5.933	282.9	4.732	10.104	5.905	282.3
	8.4	4.722	10.054	5.916	280.9	4.722	10.076	5.897	280.5
	9.3	4.713	10.025	5.903	278.9	4.718	10.035	5.885	278.6
	9.6	4.718	10.017	5.907	279.2	4.722	10.035	5.885	278.8
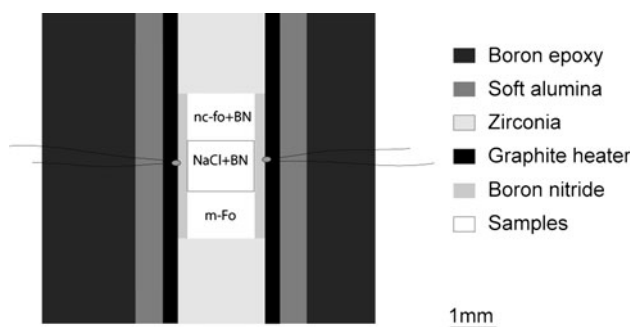
Fig. 1 Schematic of the MAP assembly

Considering the instrumental line broadening (β_i) (Willets 1965), Eq. 1 can also be written:

$$\beta^2 = \beta_o^2 - \beta_i^2 \tag{3}$$

where β_o is the observed broadening. β_i was determined experimentally from the diffraction spectra of NaCl at ambient conditions. Using Eqs. 1 and 3, we obtain:

$$\beta_o^2 = \beta_D^2 + \beta_S^2 + \beta_i^2 \tag{4}$$

The derived average crystallite size (L) of nc-Fo before experiment derived from Eq. 4 is equal to 11 ± 2 nm. No increase of this size was observed during high-pressure high-temperature experiments. The microstrain has been found to be negligible as confirmed by Fig. 3, which presents a typical nc-Fo peak profile (crosses) and its Gaussian fitting using Plot85 (red line). (021) peak was collected under 50 ton (6.5 GPa) at room temperature after

annealing. The peak shape is broad but not asymmetric showing no evidence of residual stress. The peak fitting using a Gaussian shape gives a very small residual (green line) showing a good fitting of nc-Fo peaks and an accurate determination of nc-Fo cell parameters.

Pressure, temperature and cell parameters a, b and c obtained during experiments are presented Table 1. The error on the pressure is estimated to be ± 0.1 GPa for MAP experiments and ± 0.5 GPa for DAC experiments. The temperature is accurate within 50 K, taking uncertainty of the thermocouple location and temperature gradient into account. The error on the cell parameters (a, b and c) is estimated to be ± 0.001 Å.

We fit the P–V–T data using the well-established third-order Birch-Murnaghan equation of state and the program EosFitV5.2 (Angel 2001). For this fitting, data sets from both experimental techniques were combined as we had too few experimental points using DAC to fit them separately from MAP data. A first fitting was performed with no constrained on the parameters. m-Fo exhibits a bulk modulus at zero pressure ($K_{0(\text{m-Fo})}$) of 122.9 (± 10.5) GPa while the bulk modulus at zero pressure of nc-Fo ($K_{0(\text{nc-Fo})}$) is 114.6 (± 11.1) GPa with the pressure derivative of the bulk modulus K' equal to 5.7 (± 2.8) and 6.3 (± 3.1), respectively. $K_{0(\text{nc-Fo})}$ exhibits a difference of -8.3 GPa with respect to $K_{0(\text{m-Fo})}$. For a correct comparison between $K_{0(\text{m-Fo})}$ and $K_{0(\text{nc-Fo})}$, the value of both bulk modulus should be obtained by either allowing K' to float or constraining K' to an identical and fixed value. In the present study, both K' obtained in the first fitting are among the highest values found in the literature (between 3.5 and 5.6;

Fig. 2 X-ray diffraction patterns at ambient conditions of m-Fo (*dash line*) and nc-Fo (*solid line*) and forsterite standard peaks position (*red sticks*). The subview on the upper right corner is a zoom of (131) and (112) peaks
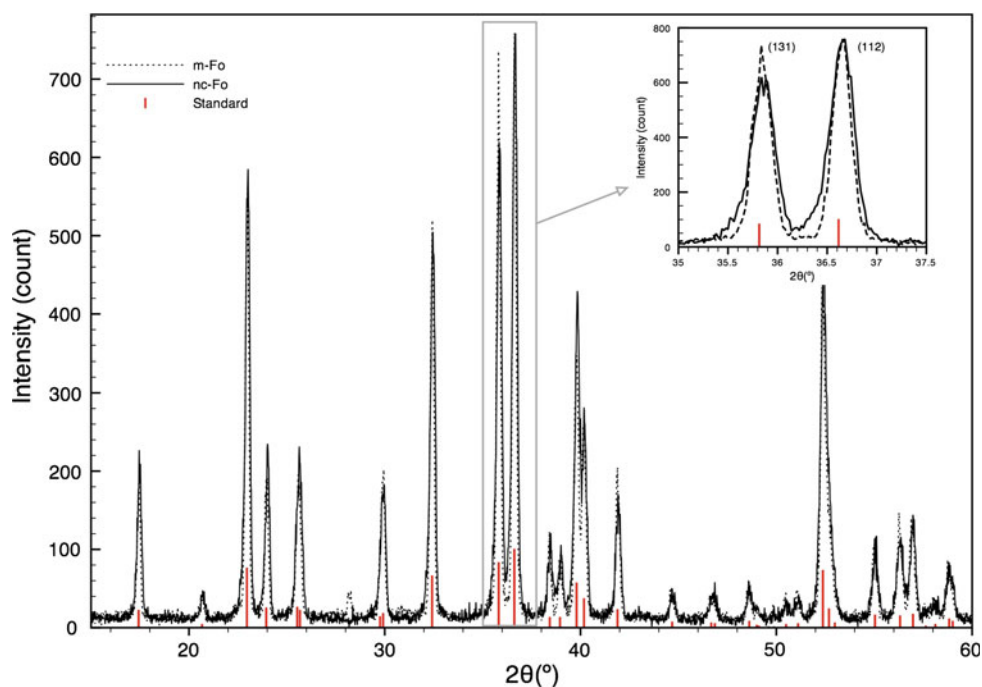
Fig. 3 nc-Fo (021) peak at 6.5 GPa and room temperature. *Red crosses* data, *red line* Gaussian fitting, *green line* residual and *black stick* measured peak position
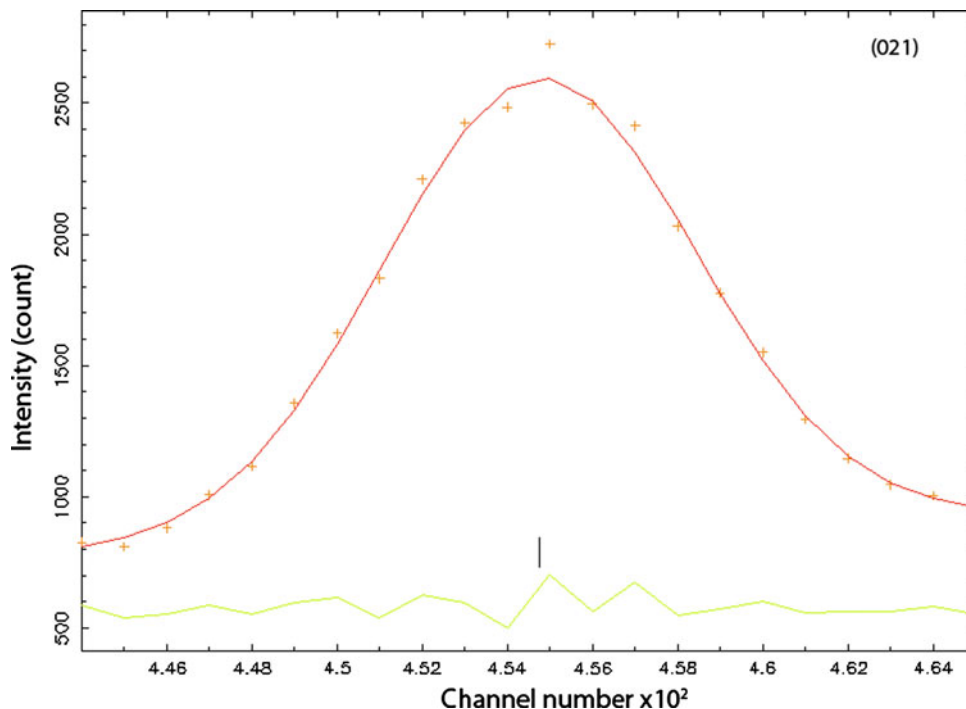
e.g. Knittle 1995; Wentzcovitch and Stixrude 1997; Zha et al. 1996, 1998a, b). Pressure derivatives might not be very well constrained due to the small pressure range explored and the tradeoff between K_0 and K'. A second fitting was then performed assuming K' is identical for m-Fo and nc-Fo. This assumption might introduce uncertainties on the K_0 values, which are not taking into account thereafter. K' has been fixed to 3.88. Brodholt et al. (1996) derived this value from ab initio calculation of compressibility of forsterite for pressures up to 70 GPa. Using $K' = 3.88$, the authors reproduce very well the experimental compression data of Will et al. (1986), Kudoh and Takeuchi (1985) and Andrault et al. (1995) over the entire experimental pressure range (up to 70 GPa).

The results of the second fitting for m-Fo and nc-Fo with K' fixed at 3.88 are shown in Table 2. Unit cell volume at zero pressure (V_0), thermal expansion parameters (α_0 and α_1) and the bulk modulus temperature derivative $(dK/dT)_P$

of m-Fo and nc-Fo are very comparable and are similar to the values found in the literature (Anderson and Isaak 1995; Fei 1995; Katsura et al. 2008; Knittle 1995 and herein references), except for α_1 and $(dK/dT)_P$ of nc-Fo. Notice the negative value calculated for $\alpha_{1(nc-Fo)}$ as well as the low magnitude of $(dK/dT)_{P(nc-Fo)}$. A confirmation of both values is necessary before commenting on the trend and the magnitude as the uncertainties associated with them are great. $K_{0(m-Fo)}$ is equal to 129.6 (±3.2) GPa, which is consistent with previously determined bulk moduli (Brodholt et al. 1996; Isaak et al. 1989; Knittle 1995; Zha et al. 1996, 1998a, b). However, $K_{0(nc-Fo)}$ remains 6.4 GPa lower than our $K_{0(m-Fo)}$ and is equal to 123.3 (±3.4) GPa. Figure 4 presents our experimental data (V/V_0 vs. pressure for the different explored temperatures) of m-Fo and nc-Fo. The solid and dashed lines represent the third-order Birch-Murnaghan equation of state fitting of m-Fo and nc-Fo, respectively.

Experimental studies (Ehm et al. 2009; Erb 1995; Mayo et al. 1990; Wang et al. 2007; Zhou et al. 2003) and theoretical simulations (Latapie and Farkas 2003; Van Swygenhoven and Caro 1998; Zhao et al. 2006) on nanocrystalline metal, alloys, ceramic and oxides have demonstrated the influence of grain size on their elastic properties. In numerous cases, elastic moduli of nanomaterial are lower than their bulk counterpart and decreases with the decreasing of grain size within a range of 2 nm to a few tens of nanometers, although their plastic behaviors may sometimes show an opposite trend (Chen et al. 2005; Zhao et al. 2007). For comparison in the same grain size range, $K_{0(nc-Fo)}$ is 4.9% smaller than $K_{0(m-Fo)}$ while K_0

Table 2 Unit cell volume at zero pressure (V_0), thermal expansion parameters (α_0 and α_1), bulk modulus at zero pressure (K_0), and bulk modulus temperature derivative (dK/dT) of m-Fo and nc-Fo for K' fixed at 3.88

	m-Fo	nc-Fo
V_0 (Å³)	290.5 ± 0.2	290.5 ± 0.3
K_0 (GPa)	129.6 ± 3.2	123.3 ± 3.4
α_0 ($\times10^{-5}$)	2.289 ± 0.247	2.471 ± 0.288
α_1 ($\times10^{-8}$)	0.114 ± 0.347	−0.316 ± 0.342
$(dK/dT)_P$	−0.011 ± 0.005	−0.004 ± 0.006

Fig. 4 Experimental
compression data of m-Fo and
nc-Fo for **a** ambient conditions
and **b** different temperatures as
function of pressure. *Crosses*
DAC data. *Diamonds and
circles* MAP data. *m*- macro-
powder forsterite data. *nc*-
nanocrystalline forsterite data.
The *solid and dashed lines*
represent the third-order Birch-
Murnaghan equation of state
that fits best m-Fo and nc-Fo
data, respectively
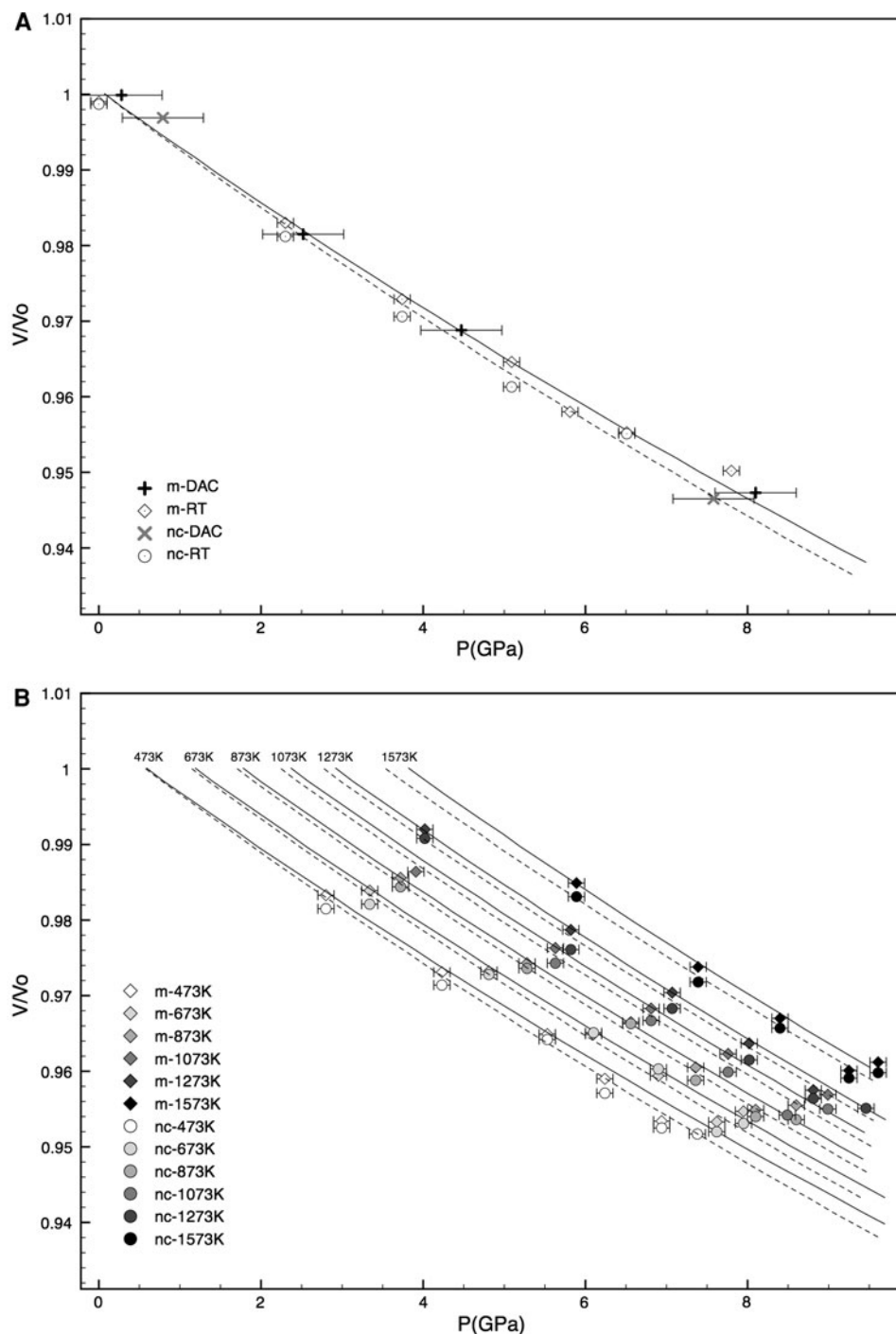
of nanocrystalline MgO is 8.3% smaller than K_0 of its bulk counterpart (Yeheskel et al. 2004), K_0 of nanocrystalline α-Al$_2$O$_3$ is similar to K$_0$ of its bulk counterpart (Zhao et al. 2001) and K_0 of nanocrystalline γ-Al$_2$O$_3$ is 34.5% smaller than K_0 of its bulk counterpart (Ahuja et al. 2004; Zhao et al. 2001). Therefore, the effect of grain size on the bulk modulus of forsterite is relatively moderate.

One of the characteristics of nano-material is a high surface area to volume ratio. This implies a significant

volume fraction of grain boundary and triple junction. Simulations on nanocrystalline α-Fe (Latapie and Farkas 2003) and Ni (Zhao et al. 2006), and experimental studies on nanocrystalline MgO (Yeheskel et al. 2004), Fe, Cu, Ni and (Cu-Ni) (Shen et al. 1995) attribute the softening of their elastic moduli to the elastic weakness of grain boundary and triple junction. Following this hypothesis, we calculate the K_0 for grain boundary and triple junction of forsterite using our data set. This is done by using a simple

rule of mixture of crystalline grain body, grain boundary and triple junction based on their volume fractions (Latapie and Farkas 2003; Paul 1960; Shen et al. 1995; Zhao et al. 2006). $K_{0(nc\text{-}Fo)}$ can be expressed as:

$$K_{0(nc-Fo)} = f_{(cg)}K_{0(cg)} + f_{(gb)}K_{0(gb)} + f_{(tj)}K_{0(tj)} \tag{5}$$

where $K_{0(cg)}$, $K_{0(gb)}$ and $K_{0(tj)}$ ($f_{(cg)}$, $f_{(gb)}$ and $f_{(tj)}$) are the bulk moduli (volume fractions) of the crystalline grain body, grain boundary and triple junction, respectively. $K_{0(cg)}$ is assumed to be equal to $K_{0(m\text{-}Fo)}$ since the contribution of grain boundaries and triple junctions is negligible for a 5 μm grain size sample. We determined the volume fractions of crystalline grain body, grain boundary and triple junction using the modified tetrakaidecahedral grain shape model proposed by Zhou et al. (2007). The grain boundary width was assumed to be 0.5 nm (Ricoult and Kohlstedt 1983). Ricoult and Kohlstedt (1983) have determined the thickness of the olivine grain boundaries using transmission electron microscopy (TEM). Zhou et al. (2003, 2007) demonstrated that $f_{(tj)}$ increases rapidly with the decreasing of grain size for grains less than 30 nm and that the relative contribution of $K_{0(tj)}$ then becomes significant. In our case, with a grain size of 11 nm and a grain boundary width of 0.5 nm and using Zhou et al. (2007) model, we calculate $f_{(gb)} = 0.130$ and $f_{(tj)} = 0.007$; therefore $f_{(tj)} \ll f_{(gb)}$ and $K_{0(tj)}$ is assumed to have a negligible contribution to $K_{0(nc\text{-}Fo)}$. $f_{(gb)}$ and $f_{(tj)}$ are then summed and represented by the volume fraction of interface $f_{(in)}$:

$$f_{(in)} = f_{(gb)} + f_{(tj)} \tag{6}$$

and Eq. 5 becomes:

$$K_{0(nc-Fo)} = f_{(cg)}K_{0(cg)} + f_{(in)}K_{0(gb)} \tag{7}$$

The calculation gives $K_{0(gb)} = 83.5$ GPa, which is smaller by 35.5% than $K_{0(cg)}$. It is important to note that the uncertainty of $K_{0(cg)}$ is very high (more than 40 GPa) due to its sensitivity to the value of $K_{0(nc\text{-}Fo)}$ and $K_{0(m\text{-}Fo)}$ and their uncertainties. The isothermal bulk modulus ($K_T = 127.4$ (± 0.4) GPa) determined by Isaak et al. (1989) from accurate measurements on a large single-crystal can also be used as $K_{0(cg)}$ in Eq. 7. In doing so, we obtain $K_{0(gb)} = 97.4$ (± 27.3) GPa, which is still smaller than $K_{0(cg)}$ by 23.5%. This calculation confirms the tendency highlighted in our study that nc-Fo is more compressible than m-Fo due to an important contribution of grains boundaries and triple junctions with higher compressibility. Molecular dynamics simulation would be a useful method to obtain a more accurate value of $K_{0(nc\text{-}Fo)}$ and therefore of $K_{0(gb)}$. For comparison with other nano-materials, $K_{0(gb)}$ of MgO is 46.8% smaller than its $K_{0(cg)}$ (Yeheskel et al. 2004) and $K_{0(gb)}$ of Ni is 9.2% smaller than its $K_{0(cg)}$ (Zhao et al. 2006).

In the context of a subducting slab, experimental studies (Burnley et al. 1991; Rubie 1984; Vaughan and Coe 1981; Yamazaki et al. 2005) and modeling (Riedel and Karato 1997) predict a large grain size reduction due to the phase transformation of the metastable olivine into ringwoodite phase. Fine-grained ringwoodite nucleates by incoherent grain boundary or by intracrystalline mechanism depending on olivine grain size (Kerschhofer et al. 1998) and this grain growth rate is slow according to Yamazaki et al. (2005). In the case of incoherent grain boundary nucleation, Burnley et al. (1991) observed using TEM that the grain size ranges from 0.5 μm to less than 10 nm in γ-Mg$_2$GeO$_4$ after phase transformation. Ten nanometers to tens of nanometer size lamellae of ringwoodite are also observed while intracrystalline mechanism takes place (Kerschhofer et al. 1996, 1998). In cold subducting slab, the rheological properties of the regions, where the olivine to ringwoodite phase transformation occurs (below 300 km) are strongly affected by the grain-size reduction and superpasticity is believed to control the deformation mechanism (Vaughan and Coe 1981). Therefore, weakening of the slab (Karato 1998; Karato et al. 1998; Riedel and Karato 1997) and deep-focus earthquake (Burnley et al. 1991; Green and Burnley 1989) result from the presence of this fine-grained ringwoodite. Grain size can also influence elastic properties of olivine as shown in the present work. If elastic behavior of ringwoodite is influenced by its grain size in a similar way to that of forsterite we observed here, the fine grain region of the subducting slab may show a slower seismic velocity.

References

Ahuja R, Osorio-Guillen MJ, Souza de Almeida J, Holm B et al (2004) Electronic and optical properties of γ-Al$_2$O$_3$ from ab initio theory. J Phys Condens Matter 16:2891–2900

Anderson OL, Isaak DG (1995) Elastic constants of mantle minerals at high temperature. In: Ahrens TJ (ed) Mineral physics and crystallography: a handbook of physical constants. American Geophysical Union, Washington DC, pp 64–97

Andrault D, Bouhifd MA, Itié JP, Richet P (1995) Compression and amorphization of (Mg, Fe)$_2$SiO$_4$ olivines: an X-ray diffraction study up to 70 GPa. Phys Chem Miner 22(2):99–107

Angel RJ (2001) EOS-FITv5.2. Crystallography laboratory. Virginia Tech, Blackburg

Baldwin K (1990) Plot85. Mineral Physics Institute, Stony Brook University, NY

Brodholt J, Patel A, Refson K (1996) An ab initio study of the compressional behavior of forsterite. Amer Miner 81:257–260

Burnley PC, Green HW II, Prior DJ (1991) Faulting associated with the olivine to spinel transformation in Mg_2GeO_4 and its implications for deep-focus earthquakes. J Geophys Res 96(B1):425–443

Chen J, Schmidt N, Chen JH, Wang LP et al (2005) Yield strength enhancement of MgO by nanocrystals. J Mater Sci 40(21):5763–5766

Decker DJ (1965) Equation of state of NaCl and its use as a pressure gauge in high-pressure research. J Appl Phys 36(1):157–161

Decker DL (1971) High-pressure equation of state for NaCl, KCl and CsCl. J Appl Phys 42(8):3239–3244

Ehm L, Michel FM, Antao SM, Martin CD et al (2009) Structural changes in nanocrystalline mackinawite (FeS) at high pressure. J Appl Cryst 42:15–21

Erb U (1995) Electrodeposited nanocrystals: synthesis, properties and industrial applications. Nanostruct Mater 6:533–538

Fei Y (1995) Thermal expansion. In: Ahrens TJ (ed) Mineral physics and crystallography: a handbook of physical constants. American Geophysical Union, Washington DC, pp 29–44

Frost HJ, Ashby MF (1982) Deformation-mechanism map. Pergamon Press, Oxford

Gerward L, Morup S, Topsoe H (1976) Particle size and strain broadening in energy-dispersive X-ray powder patterns. J Appl Phys 47(3):822–825

Green HW II, Burnley PC (1989) A new self-organizing mechanism for deep-focus earthquakes. Nature 341:733–737

Hochella MF, Lower SK, Maurice PA, Penn RL et al (2008) Nanominerals, mineral nanoparticles, and earth systems. Science 319:1631–1635

Isaak DG, Anderson OL, Goto T (1989) Elasticity of single-crystal forsterite measured to 1700 K. J Geophys Res 94(B5):5895–5906

Karato S-I (1998) Seismic anisotropy in the deep mantle, boundary layers and the geometry of mantle convection. Pure Appl Geophys 151:565–587

Karato S-I, Dupas-Bruzek C, Rubie DC (1998) Plastic deformation of silicate spinel under the transition-zone conditions of the earth's mantle. Nature 395:266–269

Katsura T, Shatskiy A, Manthilake MAGM, Zhai S et al (2008) Thermal expansion of forsterite at high pressures determined by in situ X-ray diffraction: the adiabatic geotherm in the upper mantle. Phys Earth Planet Inter 174:86–92

Kerschhofer L, Sharp TG, Rubie DC (1996) Intracrystalline transformation of olivine to wadsleyite and ringwoodite under subduction zone conditions. Science 274(5284):79–81

Kerschhofer L, Dupas C, Liu M, Sharp TG et al (1998) Polymorphic transformations between olivine, wadsleyite and ringwoodite: mechanisms of intracrystalline nucleation and the role of elastic strain. Miner Mag 62(5):617–638

Klotz S, Chervin J-C, Munsch P, Le Marchand G (2009) Hydrostatic limits of 11 pressure transmitting media. J Phys D Appl Phys 42

Knittle E (1995) Static compression measurements of equations of state. In: Ahrens TJ (ed) Mineral physics and crystallography: a handbook of physical constants. American Geophysical Union, Washington DC, pp 98–142

Kudoh Y, Takeuchi Y (1985) The crystal structure of forsterite Mg_2SiO_4 under high pressure up to 149 kb. Z Kristallogr 171:291–302

Latapie A, Farkas D (2003) Effect of grain size on the elastic properties of nanocrystalline α-iron. Scripta Mater 48:611–615

Lutterotti L, Matthies S, Wenk HR (1999) MAUD: a friendly java program for material analysis using diffraction. IUCr: Newsletter of the CPD 21(14–15)

Mao H-K, Bell PM, Dunn KJ, Chrenko RM et al (1979) Absolute pressure measurements and analysis of diamonds subjected to maximum static pressures of 1.3–1.7 Mbar. Rev Sci Instrum 50:1002

Mao H-K, Xu J, Bell PM (1986) Calibration of the ruby pressure gauge to 800 kbar under quasi-hydrostatic conditions. J Geophys Res 91:4673–4676

Mayo MJ, Siegel RW, Narayanasamy A, Nix WD (1990) Mechanical properties of nanophase TiO_2 as determined by nanoindentation. J Mater Res 5(5):1073–1082

Mueller HJ, Schilling FR, Lauterjung J, Lather C (2003) A standard-free pressure calibration using simultaneous XRD and elastic property measurements in a multi-anvil device. Eur J Miner 15:865–873

Paul B (1960) Prediction of elastic constants of multiphase materials. Trans AIME 218:36–41

Ricoult DL, Kohlstedt DL (1983) Structural width of low-angle grain boundaries in olivine. Phys Chem Miner 9:133–138

Riedel MR, Karato S-I (1997) Grain-size evolution in subducted oceanic lithosphere associated with the olivine-spinel transformation and its effects on rheology. Earth Planet Sci Lett 148:27–43

Rubie DC (1984) The olivine-spinel transformation and the rheology of subducting lithosphere. Nature 308:505–508

Saberi A, Alinejad B, Negahdari Z, Kazemi F et al (2007) A novel method to low temperature synthesis of nanocrystalline forsterite. Mater Res Bull 42:666–673

Shen TD, Koch CC, Tsui TY, Pharr GM (1995) On the elastic moduli of nanocrystalline Fe, Cu, Ni and Cu-Ni alloys prepared by mechanical milling/alloying. J Mater Res 10(11):2892–2896

Shen Y, Kumar RS, Pravica M, Nicol MF (2004) Characteristics of silicone fluid as a pressure transmitting medium in diamond anvil cells. Rev Sci Instrum 75(11):4450–4454

Van Swygenhoven H, Caro A (1998) Plastic behavior of nanophase metals studied by molecular dynamics. Phys Rev B 58(17):11246–11251

Vaughan PJ, Coe RS (1981) Creep mechanism in Mg_2GeO_4: effects of a phase transition. J Geophys Res 86(B1):389–404

Wang Y, Weidner DJ, Meng Y (1998) Advances in equation of state measurements in SAM-85. In: Manghnani MH, Yagi T (eds) Properties of earth and planetary materials at high pressure and temperature, geophysical monograph 101. American Geophysical Union, Washington DC, pp 365–372

Wang Y, Zhang J, Zhao Y (2007) Strength weakening by nanocrystals in ceramic materials. Nano Lett 7(10):3196–3199

Weidner DJ, Vaughan MT, Ko J, Wang Y (1992) Characterization of stress, pressure and temperature in SAM85, a dia type high pressure apparatus. In: Syono Y, Manghnani MH et al (eds) High-pressure research; application of the earth and planetary sciences, geophysical monograph 67. American Geophysical Union, Washington DC, pp 13–17

Weidner DJ, Wang Y, Vaughan MT (1994) Yield strength at high pressure and temperature. Geophys Res Lett 21(9):753–756

Wentzcovitch RM, Stixrude L (1997) Crystal chemistry of forsterite: a first-principles study. Amer Miner 82:663–671

Will G, Hoffbauer W, Hinze E, Laurejung J (1986) The compressibility of forsterite up to 300 kbar measured with synchrotron radiation. Physica 139 and 140B: 193–197

Willets FW (1965) An analysis of X-ray diffraction line profiles using standard deviation as a measure of breadth. Brit J Appl Phys 16:323–333

Wilson B, Dewers T, Reches Z, Brune J (2005) Particle size and energetics of gouge from earthquake rupture zones. Nature 434:749–752

Yamazaki D, Inoue T, Okamoto M, Irifune T (2005) Grain growth kinetics of ringwoodite and its implication for rheology of the subduction slab. Earth Planet Sci Lett 236:871–881

Yeheskel O, Chaim R, Shen Z, Nygren M (2004) Elastic moduli of grain boundaries in nanocrystalline MgO ceramics. J Mater Res 20(3):719–725

Zha C-S, Duffy TS, Downs RT, Mao H-K et al (1996) Sound velocity and elasticity of single-crystal forsterite to 16 GPa. J Geophys Res 101(B8):17535–17545

Zha C-S, Duffy TS, Downs RT, Mao H-K et al (1998a) Brillouin scattering and X-ray diffraction of San Carlos olivine: direct pressure determination to 32 GPa. Earth Planet Sci Lett 159:25–33

Zha C-S, Duffy TS, Downs RT, Mao H-K (1998b) Single-crystal elasticity of the alpha and beta of Mg_2SiO_4 polymorphs at high pressure. In: Manghnani MH, Yagi T et al (eds) Properties of earth and planetary materials at high pressure and temperature. American Geophysical Union, Washington DC, pp 9–16

Zhao Z, Hearne GR, Maaza M, Laher-Lacour F et al (2001) Compressibility of nanostructured alumina phases determined from synchrotron X-ray diffraction studies at high pressure. J Appl Phys 90(7):3280–3285

Zhao S-J, Albe K, Hahn H (2006) Grain size dependence of the bulk modulus of nanocrystalline nickel. Scripta Mater 55:473–476

Zhao Y, Zhang Y, Clausen B, Shen TD et al (2007) Thermomechanics of nanocrystalline nickel under high pressure-temperature conditions. Nano Lett 72:426–432

Zhou Y, Erb U, Aust KT, Palumbo G (2003) The effects of triple junctions and grain boundaries on hardness and Young's modulus in nanostructured Ni-P. Scripta Mater 48:825–830

Zhou Y, Erb U, Aust KT (2007) The role of interface volume fractions in the nanocrystalline to amorphous transition in fully dense materials. Phil Mag 87(36):5749–5761